How to cite: *Angew. Chem. Int. Ed.* **2024**, *63*, e202414984
doi.org/10.1002/anie.202414984

Osmotic Energy Conversion

Horizontal Transport in $Ti_3C_2T_x$ MXene for Highly Efficient Osmotic Energy Conversion from Saline-Alkali Environments

Han Qian, Puguang Peng, Hongzhao Fan, Zhe Yang, Lixue Yang, Yanguang Zhou, Dan Tan, Feiyao Yang, Morten Willatzen, Gehan Amaratunga, Zhonglin Wang,* and Di Wei**

Abstract: Osmotic energy from the ocean has been thoroughly studied, but that from saline-alkali lakes is constrained by the ion-exchange membranes due to the trade-off between permeability and selectivity, stemming from the unfavorable structure of nanoconfined channels, pH tolerance, and chemical stability of the membranes. Inspired by the rapid water transport in xylem conduit structures, we propose a horizontal transport MXene (H-MXene) with ionic sequential transport nanochannels, designed to endure extreme saline-alkali conditions while enhancing ion selectivity and permeability. The H-MXene demonstrates superior ion conductivity of 20.67 $S\,m^{-1}$ in 1 M NaCl solution and a diffusion current density of 308 $A\,m^{-2}$ at a 10-fold salinity gradient of NaCl solution, significantly outperforming the conventional vertical transport MXene (V-MXene). Both experimental and simulation studies have confirmed that H-MXene represents a novel approach to circumventing the permeability-selectivity trade-off. Moreover, it exhibits efficient ion transport capabilities, addressing the gap in saline-alkali osmotic power generation.

Introduction

As fossil energy reserves dwindle, there is an imperative to cultivate renewable energy sources like osmotic power, solar energy, wind energy, and others to fulfill the sustainable demands of societal advancement.[1] Osmotic energy, considered a crucial component of "blue energy," harvests energy from the salinity gradient without producing pollution or emitting carbon dioxide.[2] Theoretically, it can extract 0.8 kilowatts of energy per cubic meter, equivalent to the energy generated by water falling from a dam over 280 meters high.[3] Osmotic energy conversion relies on ion exchange membranes, where the ion dynamics determine its output performance.[4] Over the past decades, artificial nanofluidic channels inspired by biological ion channels have undergone extensive study to enhance ion dynamics in osmotic power generation.[5] For instance, one-dimensional (1D) monolayer molybdenum disulfide (MoS_2) nanopore was calculated to be able to reach the osmotic power density of 10^6 $W\,m^{-2}$ in theory when ignoring the strong pore-pore interactions.[6] Two-dimensional (2D) nanofluidic materials, such as graphene oxide (GO),[2b,7] polymeric carbon nitride (C_3N_4),[8] MXene,[9] etc., could regulate ion dynamics significantly due to their unique 2D nanofluidic channels.[10] When the dimensions of nanofluidic channels closely approximate the Debye length, ion transport within the channels becomes governed by surface charge, resulting in atypical ion

[*] H. Qian, P. Peng, Z. Yang, L. Yang, F. Yang, Prof. M. Willatzen, Prof. Z. Wang, Prof. D. Wei
Beijing Institute of Nanoenergy and Nanosystems, Chinese Academy of Sciences, Beijing 101400, People's Republic of China
E-mail: zhong.wang@mse.gatech.edu
dw344@cam.ac.uk

H. Qian, P. Peng, Z. Yang
School of Nanoscience and Engineering, University of Chinese Academy of Sciences, Beijing 100049, People's Republic of China

H. Fan, Prof. Y. Zhou
Department of Mechanical and Aerospace Engineering, The Hong Kong University of Science and Technology, Clear Water Bay, Kowloon, Hong Kong SAR, People's Republic of China

Prof. D. Tan
School of Advanced Materials and Nanotechnology, Xidian University, Xi'an 710126, People's Republic of China

Prof. D. Wei
Centre for Photonic Devices and Sensors, University of Cambridge, 9 JJ Thomson Avenue, Cambridge, CB3 0FA, UK

Prof. G. Amaratunga
Zhejiang University—University of Illinois at Urbana Champagne Institute (ZJUI) and School of Information Science and Electronics, Zhejiang University International Campus, Haining, China

Prof. G. Amaratunga
Electrical Engineering Division, Dept. of Engineering, University of Cambridge, Cambridge CB3 0FA, UK
E-mail: gehan@intl.zju.edu.cn

Prof. Z. Wang
School of Materials Science and Engineering, Georgia Institute of Technology, Atlanta, GA 30332, USA

Prof. Z. Wang
Beijing Key Laboratory of Micro-Nano Energy and Sensor, Center for High-Entropy Energy and Systems, Beijing Institute of Nanoenergy and Nanosystems, Chinese Academy of Sciences, Beijing 101400, People's Republic of China

dynamics.[11] Augmenting ion dynamics in membrane science may hold the key to optimizing osmotic power generation.[12] Furthermore, efficient osmotic energy harvesting from oceans has been achieved using diverse methods, including the synthesis of specialized membrane materials, constructing nanoconfined channels, and optimizing ionic-electronic coupling interfacial processes.[6a,13] However, the potential for osmotic energy harvesting in saline-alkali environments was frequently neglected. Inland saline-alkali lakes (soda lakes) with freshwater inflows serve as a representative of saline-alkali environments, offering conditions suitable for osmotic energy conversion.[14] In fact, the salinity levels in specific lakes exceed those of the ocean by several orders of magnitude.[15] Nevertheless, saline-alkali lakes frequently contain high levels of sodium carbonate and sodium bicarbonate, resulting in considerable alkalinity (~50 meq L^{-1}) and a high pH (~10).[14] These characteristics impose constraints on the chemical and structural stability of channels, interfaces, or membranes during the energy conversion process.[2a,16] On the other hand, the competitive relationship between membrane selectivity and permeability necessitates the effective balancing of these factors to enhance ion selectivity, fluxes, and conductivity, ultimately achieving a commercially viable osmotic power density that is generally considered exceeding 5 W m^{-2}.[6a,12a]

The continuous transpiration in vascular plants plays a pivotal role in their water-salt balance and contributes to the global water cycle. This phenomenon is attributed to the low-resistance vessel structure in the xylem, facilitating rapid water uptake.[17] This inspired investigations into ion transport directions in 2D nanofluidic materials, where ion dynamics differ significantly depending on whether ions transport horizontally or vertically through the nanosheets.[18] Horizontal ion transport may exhibit higher ion fluxes due to its ability to exploit nanoconfined channels with a high aspect ratio, similar to the transport of water and salts in the xylem of vascular plants.[17b,18a,19] Therefore, by redirecting ion transport from the vertical to the horizontal direction, ion fluxes may be enhanced while maintaining high ion selectivity, as the chemical composition of the channels remains unchanged.[20] This approach could represent an effective strategy for reconciling the trade-off between selectivity and permeability. Recently, Cao et al. have compared the ion transport differences within vertically transported graphene oxide (V-GO) and horizontally transported graphene oxide (H-GO), respectively.[20] The horizontal structure exhibited faster ionic permeability compared to the vertical structure. However, harvesting osmotic energy from saline-alkali environments requires nanochannels with enduring chemical and structural characteristics, encompassing stable layering and surface charge, qualities absent in materials such as GO. Hence, it is imperative to opt for a material proficient in effectively accommodating a wide range of pH gradients for optimal osmotic energy conversion in saline-alkali environments.

Herein, inspired by the rapid water transport observed in xylem vessel elements, we designed a horizontal transport MXene (H-MXene) prepared by simple vacuum filtration. MXene includes numerous surface terminations (–OH, –F, and =O), which offer excellent cation selectivity and help reduce the activation energy for ionic dehydration. Compared to conventional vertical transport MXene (V-MXene), our H-MXene exhibits significantly higher ionic fluxes for ultrafast ion transport through nanofluidic channels. It demonstrates an enhancement in ion conductivity of nearly five orders of magnitude and an increase in diffusion current density of about three orders of magnitude. This effectively overcomes the permeability-selectivity trade-off observed in conventional vertical transport membranes. The results show that H-MXene could achieve an osmotic power density of 9.47 W m^{-2} and an ultrahigh energy conversion efficiency of 45.7 % in NaCl solution at a 50-fold salinity gradient. Meanwhile, H-MXene maintains high ion selectivity and osmotic power density in HCl and NaOH solutions with varying salinity gradients, ensuring stable osmotic energy conversion in acidic and alkaline environments. The diffusion of various cations in both horizontal and vertical ion transport channels was theoretically simulated to corroborate the experimental findings. These results offer a solution to the challenge of the permeability-selectivity trade-off in ion-exchange membranes and encourage further exploration of osmotic power generation from saline-alkali environments.

Results and Discussion

Fabrication and Characterization of $Ti_3C_2T_x$ MXene

Figure 1a shows the fabrication process of MXene, where MXene nanosheets were obtained by selectively etching Al atoms from the Ti_3AlC_2 (MAX phase) using Li/HCl etchant, as previously reported.[9b,21] A clear Tyndall effect was observed in the diluted colloidal suspension of MXene, indicating good dispersibility. The particle size distribution demonstrated that the average particle size of MXene nanosheets was 91.33 μm, which was essential for the construction of 2D nanofluidic channels with uniform and orderly arrangements (Figure S1, Supporting Information). Finally, a uniform and flexible MXene film was obtained through simple vacuum filtration (Figures S2–S5, Supporting Information). As shown in Figure S6 (Supporting Information), ultrathin MXene nanosheets were observed on a silicon substrate. From the scanning electron microscope (SEM) image and transmission electron microscope (TEM) image, it can be observed that the MXene membrane was composed of stacked layers of nanosheets (Figures 1b,c, and S7–S9, Supporting Information). Atomic force microscope (AFM) observations indicated a lateral size distribution of these MXene nanosheets ranging from 1 to 3 μm, with an average height of 2 nm (Figure S10, Supporting Information). X-ray diffraction (XRD) patterns indicated that the (002) peak may represent the interlayer spacing of the MXene, and the layer distance was calculated as ~13.47 Å. While in a hydrated state, the XRD pattern shows that the (002) peak of the MXene membrane shifted to a lower angle, resulting from the fact that water molecules might be inserted into layer spacing between the nanosheets. As a

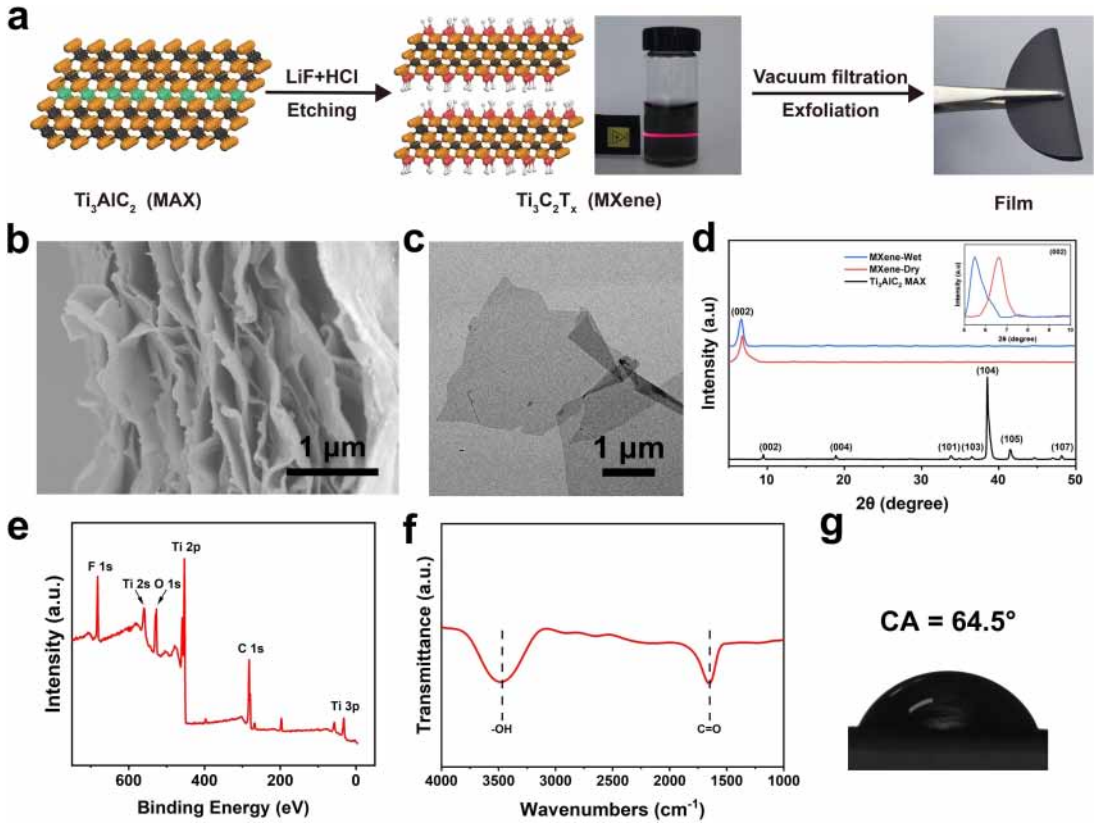

Figure 1. Preparation and characterization of MXene. a) The fabrication process of MXene. b) Cross-sectional SEM image of MXene exhibiting packed lamellar structures. c) TEM image of the exfoliated MXene nanosheets. d) XRD patterns of MAX phase Ti_3AlC_2 powder and $Ti_3C_2T_x$ lamellar membrane. The inset shows a clear difference between ambient and fully hydrated MXene membranes in low Bragg angle pattern, indicating its swelling behavior in water. e) XPS spectrum of MXene membrane. f) FTIR spectrum indicates the terminal functional groups in synthetic MXene. g) The MXene membrane is hydrophilic, with surface contact angles of 64.5°.

result, the interlayer spacing (d) in a hydrated state was 16.10 Å (Figure 1d). Considering the theoretical thickness (a) of a single layer of MXene is approximately ~9.8 Å,[9a] the estimated space for ion diffusion is $\delta = (d\text{-}a) \approx 6.3$ Å. In addition, the terminal functional groups were examined by X-ray photoelectron spectroscopy (XPS), Fourier-transform infrared spectroscopy (FTIR), and Raman spectroscopy, as shown in Figures 1e,f, and S11–12 (Supporting Information). The XPS spectra showed that abundant surface terminal groups, including –O, –OH, and –F, were bonded to the surface of Ti_3C_2 nanosheets.[22] These functional groups, as evidenced by Raman spectra and FTIR as well,[23] ensured the MXene membranes hydrophilic and negatively charged (Figures 1g and S13, Supporting Information). Furthermore, the prepared MXene membrane can remain stable in both deionized water and saline-alkali environments for over one month, which is highly significant for future practical osmotic applications (Figures S14–S17, Supporting Information).

Highly Efficient Osmotic Energy Conversion of H-MXene

Initially, the osmotic energy conversion capability of H-MXene was evaluated in artificial seawater and river environment of 0.5 M/0.01 M salinity gradient NaCl solutions, as commonly used in previous reports.[20,24] The H-MXene osmotic power source was made by placing the prepared MXene membrane in an acrylic device with the confined acrylic tape to prevent the solution from leaking (Figure 2a). Ag/AgCl standard electrodes were used to eliminate the contribution of redox reactions.[9c,25] The negatively charged nanoconfined channels of the H-MXene enabled the selective transport of cations (Na^+), which can generate a membrane potential of 96.6 mV and a diffusion current of 11.42 μA at 50-fold salinity gradient (Figure 2b). The osmotic power density (P) is determined by $P = I_{sc}^2 \times R_M$ (where the I_{sc} is the diffusion current and R_M is the membrane resistance). When the load resistance R_L equals the membrane resistance R_M, the power achieves its peak value.[26] The power generation performance increases and the diffusion current decreases with the increasing external load resistance R_L, indicating that the osmotic power source exhibits typical Ohm-type performance. When the external load resistance was 9.02 kΩ, the osmotic power density of the H-MXene osmotic power source reached its maximum value of 9.47 $W m^{-2}$ (Figure 2c). It achieved ultra-low membrane internal resistance at thicknesses of 3 mm by transporting ions vertically. In comparison with the performance reported in other articles under the same salinity

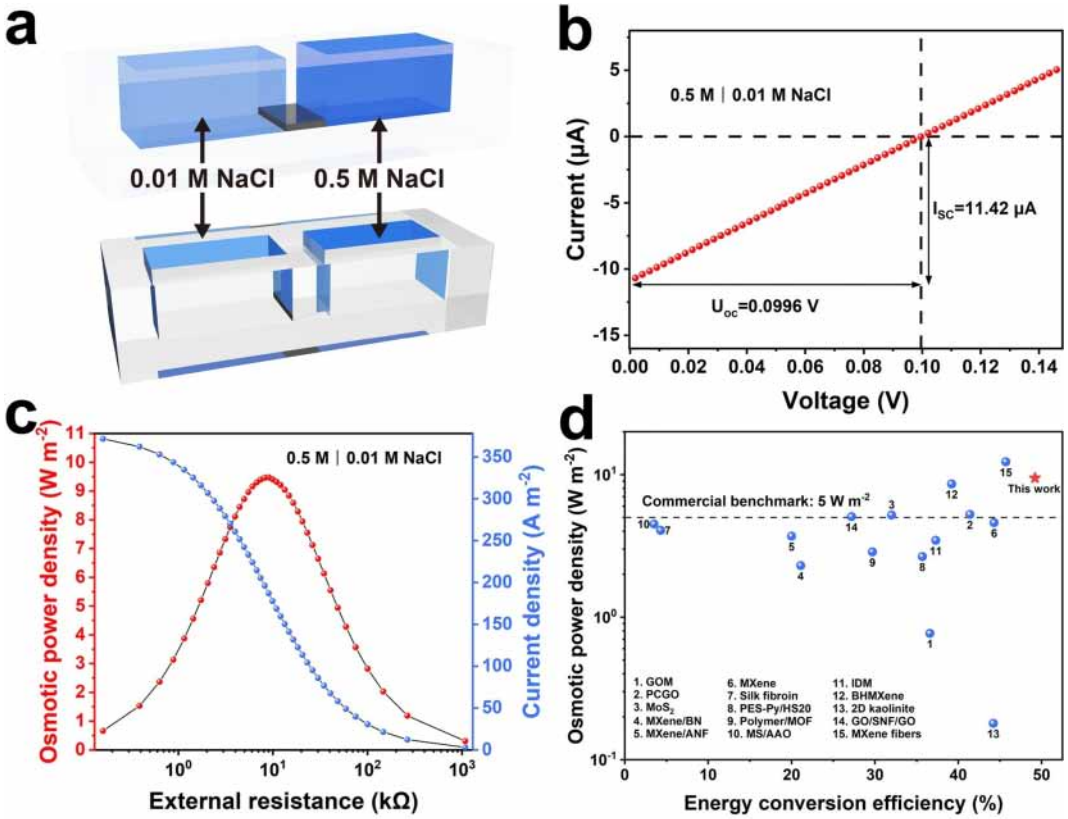

Figure 2. The ion transport performance of H-MXene osmotic power source at 0.5 M/0.01 M salinity gradient NaCl solutions. a) Schematic of energy harvesting from the seawater and river water (the black rectangle is the H-MXene). b) I–V curve of H-MXene osmotic power source at 0.5 M/0.01 M salinity gradient NaCl solutions. c) Osmotic power density and diffusion current density as a function of external resistance. The obtained osmotic power density of the H-MXene osmotic power source is as high as 9.47 W m^{-2}. d) Comparison of the H-MXene osmotic power source with other reported osmotic power sources for the osmotic power density and energy conversion efficiency.

gradient of 0.5 M/0.01 M NaCl solutions, H-MXene osmotic power source exceeded the commercialization benchmark of 5.0 W m^{-2} and had a very high energy conversion efficiency (Figure 2d).

High Permeability and Selectivity of H-MXene

To explore the reasons for the high performance of H-MXene in osmotic energy conversion, we systematically investigated and compared the permeability and ion selectivity of V-MXene and H-MXene.[9a,c] To eliminate the interference of other factors, we prepared V-MXene and H-MXene with the same conditions for the next electrochemical tests. Although V-MXene and H-MXene have the same interlayer spacing, surface properties, and chemical composition, their transport pathways of ions are fundamentally different, resulting in differences in ionic fluxes.[19] When ions pass through V-MXene, they must traverse a 'zigzag' path through the gaps between adjacent layers. In the case of H-MXene, most ions could directly traverse a single nanochannel within the structure or traverse several adjacent nanochannels without passing through all nanochannels, resulting in shorter trajectory lengths compared to the V-MXene structure (Figure 3a). The ionic conductivities of V-MXene and H-MXene in NaCl solutions of different salinity gradients were measured by using a pair of Ag/AgCl standard electrodes (Figure 3b). When the salinity gradient of NaCl was between 1 M and 10^{-3} M, the ionic conductivity exhibited electric field induced ion transport behavior as same as the bulk solution. As the salinity gradient decreased to below 10^{-4} M, the ionic conductivity became independent of the ionic concentrations and was governed by surface-charge-controlled ion transport. In this regime, the thickness of the electrical double layer increased and became comparable to the dimension of the nanochannel.[27] Consequently, the negatively charged MXene nanochannels exhibit selective and rapid transport of cations controlled by surface charge, while anions might be excluded from the nanochannels. Furthermore, a comparison of the ionic conductivities of V-MXene and H-MXene demonstrates that the normalized ionic conductivity of H-MXene surpasses that of V-MXene by nearly five orders of magnitude across a wide range of salinity gradient conditions. Moreover, the membrane potential (U_{oc}) of H-MXene increased from 0.057 mV to 0.173 mV when the salinity gradient of NaCl solution was varied from 10-fold to 1000-fold, corresponding to cation transference numbers (t_+) of 0.982 and 0.988, respectively. This indicated that H-MXene could maintain a high degree of cation selectivity under high

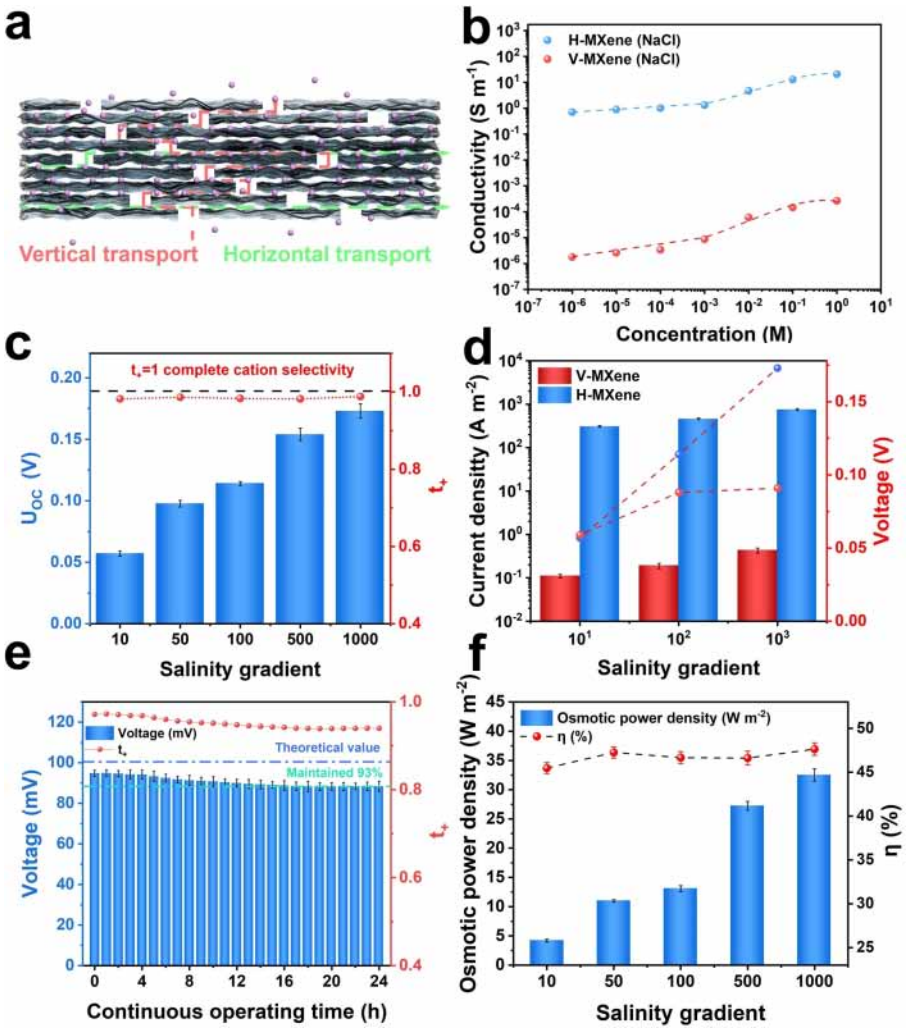

Figure 3. High permeability and selectivity of H-MXene osmotic power source. a) Schematic of ion transport in V-MXene and H-MXene osmotic power sources. b) The ionic conductivity of H-MXene osmotic power source is five orders of magnitude higher than that of V-MXene osmotic power source. c) The U_{oc} and t_+ of H-MXene osmotic power source at different NaCl salinity gradients. d) The diffusion current density and U_{oc} of V-MXene and H-MXene osmotic power sources at different NaCl salinity gradients. e) H-MXene osmotic power source can maintain stable performance in 0.5 M/0.01 M salinity gradient NaCl solutions for 24 h. f) The osmotic power density and η of H-MXene osmotic power source at different NaCl salinity gradients.

salinity gradients (Figure 3c). However, a significant decrease in U_{oc} and t_+ were observed in V-MXene, which may be due to the ion concentration polarization effects in this structure. (Figure S18, Supporting Information).[28] The corresponding energy dispersive X-ray spectroscopy (EDS) mapping showed that the MXene nanochannels contained much more potassium than bromine (Figure S19, Supporting Information), further indicating cation selectivity. Furthermore, we illustrated the discrepancies between H-MXene and V-MXene through SEM and corresponding elemental mappings in the permeability test. H-MXene and V-MXene samples were prepared with 10 μL of 0.1 M KBr solution dropped on one side, followed by rapid removal and drying through heating to study the ion dynamics. SEM images and elemental mapping revealed the distribution of K and Br elements on the side where the solution was dropped for both H-MXene and V-MXene (Figures S20a and S20c, Supporting Information). Additionally, the side of H-MXene without dropping KBr solution exhibited a distribution of K and Br elements, with K being more abundant than Br, attributed to the cation selectivity of MXene (Figure S20b, Supporting Information). Due to differences in ion transport performance between H-MXene and V-MXene, only minimal amounts of K and Br elements were distributed on the other side of V-MXene. This indicated that even with a shorter distance required for ion diffusion (length in H-MXene: 5 mm, length in V-MXene: 6 μm), V-MXene still exhibited poorer permeability than H-MXene (Figure S20d, Supporting Information). Thus, the diffusion current density and osmotic power density in H-MXene driven by the salinity gradient were enhanced significantly by over three orders of magnitude surpass those in V-MXene as shown in Figures 3d and S21 (Supporting Information). To gain deeper insights into the distinctions

between H-MXene and V-MXene, we have supplemented electrochemical impedance spectroscopy (EIS) test. It revealed that under identical conditions, the solution resistance (R_s) of V-MXene was twice as high as that of H-MXene, indicating that the H-MXene nanochannels offer lower resistance to cation diffusion (Figure S22, Supporting Information). We further analyzed the stability of the cation selectivity of H-MXene under a 50-fold NaCl salinity gradient. The initial U_{oc} was 94.76 mV, and the corresponding t_+ was 0.972, which was very close to the theoretical value. After 24 h, U_{oc} and t_+ could still maintain 88.38 mV and 0.940, respectively, with a voltage drop within 10 %, demonstrating excellent stability (Figure 3e). Besides, from the osmotic power density and energy conversion efficiency plots of H-MXene at different salinity gradients, it can be observed that as the salinity gradient increased, the osmotic power density gradually increased from 4.19 $W m^{-2}$ to 32.52 $W m^{-2}$, and the energy conversion efficiencies remained stable and exceeded 45 % (Figure 3f). Meanwhile, H-MXene also achieved high performance in other salinity gradients, including LiCl, NaCl, KCl, and even some divalent cations (Figures S23 and S24, Supporting Information). Consistent with previous research, the results also showed that higher mobility of cations can effectively increase the diffusion current and membrane potential.[20]

Ion Transport Performance from Saline-Alkali Environment

To further validate the ion transport performance of H-MXene from saline-alkali environments, solutions of HCl and NaOH with the same salinity gradient as NaCl were used to simulate saline-alkali conditions. As depicted in Figures 4a,b, in extreme acidic environments, H-MXene exhibited lower cation selectivity and ionic currents compared to seawater-river water environments and became more pronounced with increasing salinity gradient, but it still had a diffusion current density over 1000 $A m^{-2}$ even at 1000-fold HCl salinity gradient. Conversely, in highly alkaline environments, the ion selectivity and diffusion current of H-MXene could remain stable (Figures 4c,d). H-MXene consistently demonstrates certain osmotic output in acidic and alkaline environments, which can be attributed to the spontaneous ion transport dynamics on the surface of the MXene channels. In detail, H-MXene could undergo a spontaneous deprotonation process under neutral conditions as follows:[28–29]

$$(Ti_3C_2)_n(OH)_x(O^-)_yF_z + aH_2O \rightarrow (Ti_3C_2)_n(OH)_{x-a}(O^-)_{y+a}F_z + aH_3O^+ \quad (1)$$

This process could result in more negative charges on the nanochannel surface, which could improve the cation selectivity of H-MXene. In addition, under acidic conditions, H-MXene could undergo a protonation process, as shown by the following equation:[28,30]

$$(Ti_3C_2)_n(OH)_{x-a}(O^-)_aF_z + aH_3O^+ \rightarrow (Ti_3C_2)_n(OH)_xF_z + aH_2O \quad (2)$$

In this situation, the electronegativity of the H-MXene nanochannel will decrease, which will affect the cation selectivity.[28] On the contrary, the deprotonation process of H-MXene could be further enhanced under alkaline conditions, potentially resulting in improved ion selectivity, as shown by the following equation:[30]

$$(Ti_3C_2)_n(OH)_xF_z + aOH^- \rightarrow (Ti_3C_2)_n(OH)_{x-a}(O^-)_aF_z + aH_2O \quad (3)$$

Additionally, we supplemented the surface charge density testing under different pH conditions using Kelvin probe force microscope (KPFM) to further analyze the mechanism and process. We directly observed the mechanism in surface potential of MXene nanosheets after treatment in different pH solutions (Figure S25, Supporting Information). The calculated average potential values of MXene nanosheets were shown in Table S3 as 0.792 V (pH = 1), 0.554 V (pH = 7), and 0.359 V (pH = 13), respectively. The results indicated that there are relative differences in the average potential of MXene nanosheets, with lower average potential values observed at higher pH values. The consistent trend in the change of microscopic surface potential with the change in Zeta potential, deeply demonstrates the mechanism and process of H-MXene's ion selectivity from saline-alkali environments.

Meanwhile, it could also be observed from Figures 4a,c that the diffusion currents were enhanced regardless of acidic or alkaline conditions, and the current enhancement is more obvious under acidic conditions. The XRD measurements presented in Figures S26 and S27 (Supporting Information) also revealed the incremental interlayer spacing of H-MXene membranes under neutral, alkaline, and acidic conditions. The calculated interlayer spacings were 15.737 Å, 16.268 Å, and 16.089 Å, respectively, indicating enhanced ion transport and flux under varying conditions. Under acidic conditions, the faster migration of H^+ ions compared to Na^+ ions, owing to their smaller size, more compact structure, and lighter mass, results in enhanced permeability within the confined space.[31] Under alkaline conditions, although H-MXene nanochannels primarily facilitate cation transport, a small number of anions will still be present in the nanochannels, impeding the transport of cations. This blocking effect becomes more pronounced as the radius of the anion increases ($OH^- < Cl^-$), resulting in differences in permeability.[31a,32] Therefore, even under alkaline conditions, H-MXene could still pump Na^+, making it particularly suitable for osmotic power generation in saline-alkali environments. Finally, we measured the osmotic power density and energy conversion efficiency of H-MXene under the three conditions (Figures 4b,d). Under 10-fold and 100-fold HCl salinity gradients, the osmotic power densities were significantly improved compared to the same salinity gradient NaCl solution, increasing from 4.19 $W m^{-2}$ to 8.68 $W m^{-2}$ and from 9.47 $W m^{-2}$ to 28.02 $W m^{-2}$, respec-

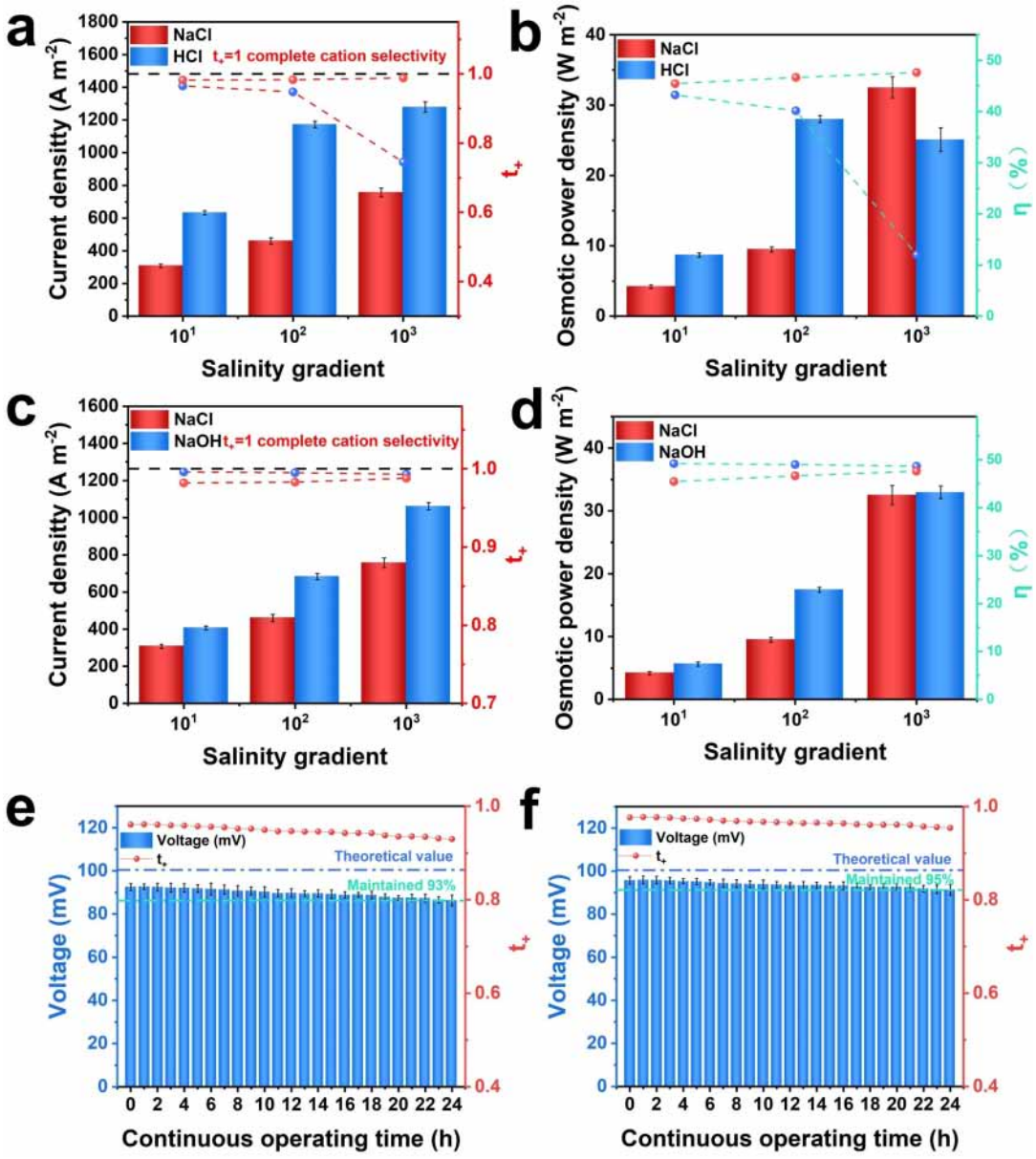

Figure 4. The detailed data analysis of H-MXene osmotic power source for illustrating ion selectivity in saline-alkali environments. a) The diffusion current density and t_+ of H-MXene osmotic power source at different salinity gradients of NaCl and HCl solutions. b) The osmotic power density and η of H-MXene osmotic power source at different salinity gradients of NaCl and HCl solutions. c) The diffusion current density and t_+ of H-MXene osmotic power source at different salinity gradients of NaCl and NaOH solutions. d) The osmotic power density and η of H-MXene osmotic power source at different salinity gradients of NaCl and NaOH solutions. e) H-MXene osmotic power source can maintain stable performance in 0.5 M/0.01 M salinity gradient HCl solutions for 24 h. f) H-MXene osmotic power source can maintain stable performance in 0.5 M/0.01 M salinity gradient NaOH solutions for 24 h.

tively. However, when the salinity gradient was increased to 1000-fold, the osmotic power density of H-MXene in HCl solution decreased, even lower than that in 100-fold HCl solutions, primarily due to the concentration polarization effect caused by the ion buildup on the membrane side, resulting in a decrease in ion selectivity.[9a,33] Thus, H-MXene showed a less energy conversion efficiency of 12.0 % under the acidic condition. In contrast, H-MXene in NaOH solution demonstrated consistent electrochemical performance across all three salinity gradients. Under the salinity gradient of 1 M/10^{-3} M, it achieved an osmotic power density of 32.95 W m^{-2} and an energy conversion efficiency of 48.67 %. This performance can be attributed to the combined effects of H-MXene's selectivity and permeability. Furthermore, by comparing the performance of H-MXene and V-MXene under acidic and alkaline conditions, it can be found that, similar to the neutral condition, the diffusion current density in H-MXene driven by the salinity gradient also exceeded that in V-MXene by three orders of magnitude (Figures S28 and S29, Supporting Information).

Both the osmotic power densities and energy conversion efficiencies of V-MXene under acidic and alkaline conditions showed similar trends to those of H-MXene (Figures S30 and S31, Supporting Information). The stability of H-MXene under 50-fold HCl and NaOH salinity gradients was also explored. Under the HCl salinity gradient, H-MXene exhibited a similar stability to that of the NaCl salinity gradient, with a retention rate of t_+ close to 93 % (Figure 4e). In contrast, under the NaOH salinity gradient, the initial U_{oc} of H-MXene was 95.74 mV, corresponding to a t_+ of 0.977, which was higher than that of the NaCl system. After 24 h, the U_{oc} and t_+ could still maintain at 91.25 mV and 0.954, respectively, with a voltage drop less than 5 %, demonstrating excellent stability (Figure 4f). Importantly, the membrane potential of H-MXene did not show obvious attenuation after 7 days, indicating excellent working stability in saline-alkali environments (Figure S32, Supporting Information).

Modeling of Cation Migration for V-MXene and H-MXene

To validate the aforementioned experimental results, theoretical simulations were conducted to elucidate the mechanism of cation transport in both V-MXene and H-MXene. Further detailed information can be found in the Supporting Information, specifically Note 8 (Supporting Information). Ion transport under a 50-fold salinity gradient was analyzed in a confirmed continuum-based framework. This framework consists of the Poisson-Nernst-Planck (PNP) equation. The two models, V-MXene and H-MXene, consist of vertically and horizontally assembled flakes with identical geometrical dimensions, respectively (Figure S33, Supporting Information). Based on the XRD results, the approximate interlayer spacing was set to 6.3 Å. Consequently, the size of the simulated 2D nanofluidic channel model was established as 1 nm. The surface charge density (σ) of the 2D nanosheets was $-0.02\ mC\,m^{-2}$, which is consistent with literature report.[9b] As shown in Figures 5a,e, the ion concentration distributions were calculated under the 0.5 M/0.01 M salinity gradient NaCl solution, and most of the models exhibited excellent ion selectivity. The thickness of the electrical double layer (EDL) was calculated to be ~0.5 nm (0.5 M NaCl, 25 °C), indicating that the EDL overlapped completely in the MXene nanochannels. Since the net diffusion current stems only from the charge separation and concentration distribution within the EDL, the completely overlapped EDL can effectively promote the ion selectivity of the nanochannel and improve the energy conversion efficiency. In addition, we explored and compared the ion transport behaviors at 1 nm, 3 nm, and 6 nm nanochannel sizes. The results demonstrated that the smaller 1 nm nanochannel exhibited superior ion selectivity compared to larger sizes. This phenomenon might arise from the decreased range of the overlapped EDLs in large nanochannels, leading to a diminished local concentration gradient. This suggested that nano-sized channels may mitigate the effect of counter-ion input into the nanochannel, thereby enhancing osmotic transport. Meanwhile, upon comparing V-MXene and H-MXene with identical nanochannel sizes, it was observed that the permeability of H-MXene was superior. Additionally, when the nanochannel size of V-MXene was too large (Figure 5f), the distribution of cations at the same diffusion time indicated poorer permeability relative to H-MXene (Figure 5c).

We further performed typical molecular dynamics (MD) simulations to investigate the ion transport behaviors through MXene membranes under different environments, aiming to elucidate the underlying reasons for the ultrafast ion permeation observed in H-MXene. We constructed atomic models of MXene with an interlayer spacing of ~1 nm, and the surface charge density and elemental

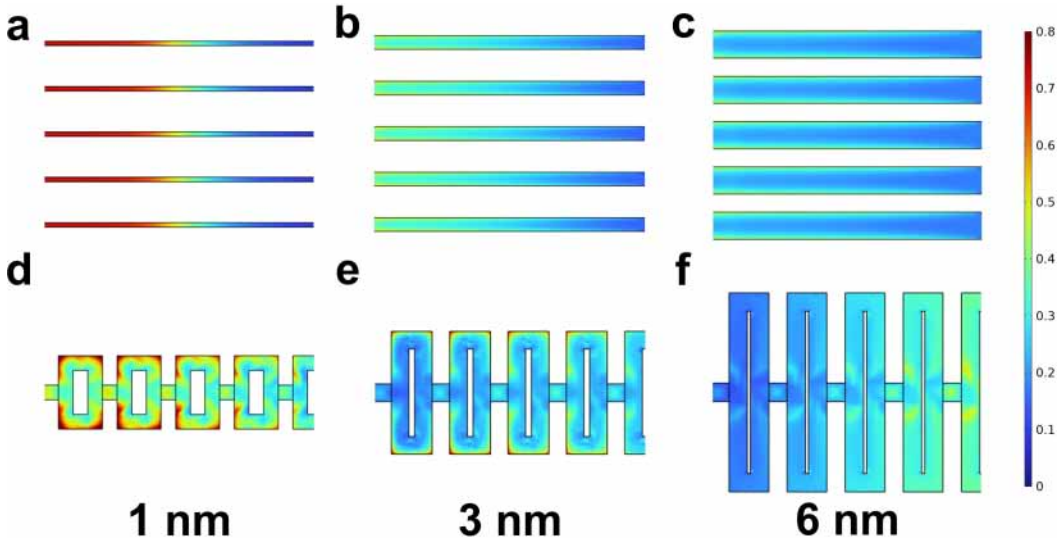

Figure 5. Numerical simulation of the ionic concentration profiles of cations based on 2D nanofluidic channels at the 0.5 M/0.01 M salinity gradient NaCl solutions. a–c) H-MXene osmotic power source with three different nanochannel sizes. d–f) V-MXene osmotic power source with three different nanochannel sizes.

composition were similar to those of experimental samples (Figures 6a and S34, Supporting Information). Initially, we compared the ion selectivity under different conditions, and simulation snapshots indicated that all MXene nanochannels exhibit excellent cation selectivity (Figures S35 and S36, Supporting Information). Additionally, hydrated ions, particularly H^+ with smaller diameters, demonstrated significantly faster mobility than Na^+ in NaCl solution or NaOH solution. In the simulations, the diffusion coefficients of Na^+ (NaOH) in H-MXene and V-MXene were 0.0408 $nm^2 ps^{-1}$ and 0.0088 $nm^2 ps^{-1}$, respectively, with the former being considerably higher than the latter (Figure 6b). This trend is consistent with the diffusion coefficients obtained from experimental calculations (Figure 6c). Furthermore, the transport rates of Na^+ (NaOH), Na^+ (NaCl), and H^+ (HCl) in H-MXene normalized by surface area were 2.57, 2.45, and 2.32 times higher, respectively, than those in V-MXene (Figure 6d). This primarily stems from the different transport pathways through H-MXene and V-MXene. The ions must take a 'zigzag' trajectory through gaps between adjacent layers in V-MXene, while most ions can directly pass through a single nanochannel within H-MXene (Figures 6a and S37, Supporting Information). As a consequence, the effective ion average velocity along the permeation direction of Na^+ (NaOH) in V-MXene is significantly reduced, which is more than 2.20 times lower than that in H-MXene (Figure 6e). Another pivotal factor contributing to the exceptionally high ion permeation is the rapid nanochannel provided by the unique geometry of H-MXene. The convoluted geometry in V-MXene generates formidable barriers, making it easier for Na^+ (NaOH) to enter the interior of H-MXene. The MD simulations revealed that the loading time (the time for ions to enter the nanochannel from the external region) in V-MXene is 2.19 times longer than that of H-MXene in NaOH system (Figure 6f). It is noteworthy that due to the limitation of computational capacity, the proportion of the entrance area of V-MXene in the simulations is much larger than in experiments. Consequently, the difference in ion transport performance between H-MXene and V-MXene in the simulations is underestimated compared to experimental observations.

Conclusion

In conclusion, the horizontal ion transport MXene featuring cation-selective nanochannels holds promising potential for osmotic power generation across various salinity gradients, particularly in saline-alkali environments. Both H-MXene and V-MXene were prepared under identical fabrication conditions to ensure they possess identical interlayer spacing and chemical composition. This consistency ultimately accounts for the comparative assessment of ion selectivity observed in both H-MXene and V-MXene. In the osmotic energy conversion system using simulated seawater and artificial river water, the H-MXene can obtain an enhanced ion conductivity of 20.67 $S m^{-1}$ in 1 M NaCl solution, which is nearly five orders of magnitude higher than conventional V-MXene under similar operating conditions. In addition, MXene could achieve stable osmotic energy conversion in simulated saline-alkali environments. In alkaline NaOH solution, the enhancement in surface charge and interlayer spacing further optimized the selectivity and permeability of MXene, achieving a maximum osmotic power density of 32.95 $W m^{-2}$ with an ultra-high energy conversion efficiency of 48.67 % at a 1000-fold salinity gradient. This work establishes a paradigm for addressing the permeability-selectivity trade-off in ion-exchange membranes and advances the field of osmotic power generation from saline-alkali environments.

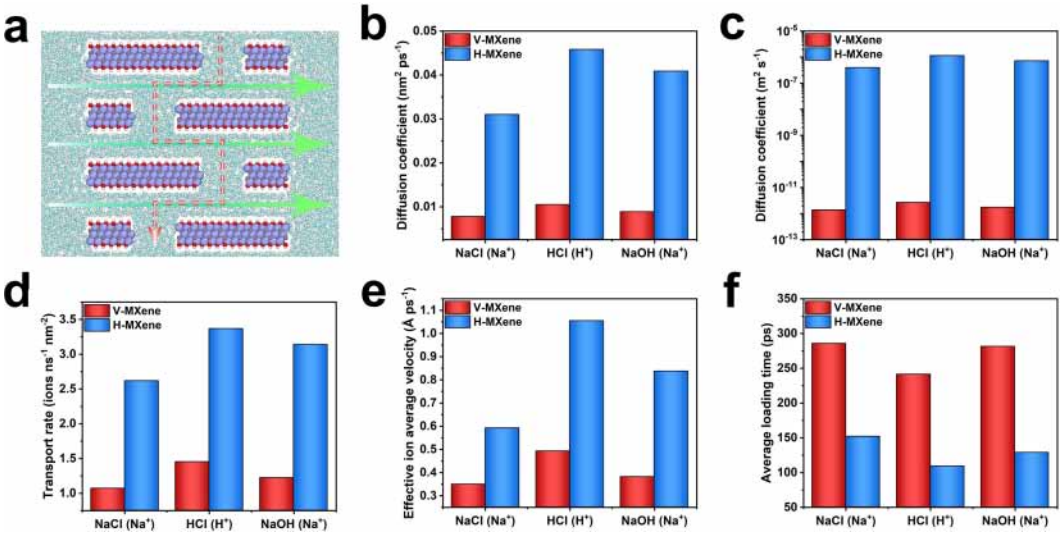

Figure 6. MD simulations of ionic transport through H-MXene and V-MXene. a) Schematic of ion transport in V-MXene (red line) and H-MXene (green lines) nanochannels. b) Simulated ion diffusion coefficients through the MXene nanochannels. c) Calculated ion diffusion coefficients through the MXene nanochannels. d) The transport rate of ions in H-MXene and V-MXene. e) The effective ion average velocity in H-MXene and V-MXene. f) The average loading time of ions in H-MXene and V-MXene.

Acknowledgements

This work was supported by the Beijing Natural Science Foundation (Grant No. IS23040). This work was supported by the National Natural Science Foundation (Grant No. 22479016).

Conflict of Interest

The authors declare no conflict of interest.

Data Availability Statement

The data that support the findings of this study are available from the corresponding author upon reasonable request.

Keywords: $Ti_3C_2T_x$ MXene · Osmotic Energy · Nanoconfined Channels · Horizontal Transport · Saline-alkali Environments

[1] a) S. Pacala, R. Socolow, *Science* **2004**, *305*, 968–972; b) S. Chu, A. Majumdar, *Nature* **2012**, *488*, 294–303; c) X. Tian, Y. Zhang, R. Zheng, D. Wei, J. Liu, *Sustain. Energy Fuels* **2020**, *4*, 2087–2113; d) H. E. Unalan, Y. Yang, Y. Zhang, P. Hiralal, D. Kuo, S. Dalal, T. Butler, S. N. Cha, J. E. Jang, K. Chremmou, G. Lentaris, D. Wei, R. Rosentsveig, K. Suzuki, H. Matsumoto, M. Minagawa, Y. Hayashi, M. Chhowalla, A. Tanioka, W. I. Milne, R. Tenne, G. A. J. Amaratunga, *IEEE Trans. Electron Devices* **2008**, *55*, 2988–3000.

[2] a) K. Xiao, L. Jiang, M. Antonietti, *Joule* **2019**, *3*, 2364–2380; b) L. Yang, F. Yang, X. Liu, K. Li, Y. Zhou, Y. Wang, T. Yu, M. Zhong, X. Xu, L. Zhang, W. Shen, D. Wei, *PNAS* **2021**, *118*, e2023164118.

[3] B. E. Logan, M. Elimelech, *Nature* **2012**, *488*, 313–319.

[4] a) X.-Y. Kong, L. Wen, L. Jiang, *Trends Chem.* **2020**, *2*, 180–182; b) R. E. Pattle, *Nature* **1954**, *174*, 660–660; c) P. Peng, F. Yang, Z. Wang, D. Wei, *Adv. Energy Mater.* **2023**, *13*, 2302360.

[5] a) A. Siria, P. Poncharal, A.-L. Biance, R. Fulcrand, X. Blase, S. T. Purcell, L. Bocquet, *Nature* **2013**, *494*, 455–458; b) J. Feng, M. Graf, K. Liu, D. Ovchinnikov, D. Dumcenco, M. Heiranian, V. Nandigana, N. R. Aluru, A. Kis, A. Radenovic, *Nature* **2016**, *536*, 197–200.

[6] a) Z. Zhang, L. Wen, L. Jiang, *Nat. Rev. Mater.* **2021**, *6*, 622–639; b) L. Wang, Z. X. Wang, S. K. Patel, S. H. Lin, M. Elimelech, *ACS Nano* **2021**, *15*, 4093–4107; c) J. Yang, B. Tu, M. Fang, L. Li, Z. Tang, *ACS Nano* **2022**, *16*, 13294–13300; d) J. Su, D. Ji, J. Tang, H. Li, Y. Feng, L. Cao, L. Jiang, W. Guo, *Chin. J. Chem.* **2018**, *36*, 417–420; e) L. Cao, Q. Wen, Y. Feng, D. Ji, H. Li, N. Li, L. Jiang, W. Guo, *Adv. Funct. Mater.* **2018**, *28*, 1804189.

[7] a) D. Wei, F. Yang, Z. Jiang, Z. Wang, *Nat. Commun.* **2022**, *13*, 4965; b) Y. Ouyang, X. Li, S. Li, P. Peng, F. Yang, Z. L. Wang, D. Wei, *Nano Energy* **2023**, *116*, 108796; c) F. Yang, P. Peng, Z.-Y. Yan, H. Fan, X. Li, S. Li, H. Liu, T.-L. Ren, Y. Zhou, Z. L. Wang, D. Wei, *Nat. Energy* **2024**, *9*, 263–271; d) D. Wei, *Sci. Rep.* **2015**, *5*, 15173.

[8] a) K. Xiao, P. Giusto, L. Wen, L. Jiang, M. Antonietti, *Angew. Chem. Int. Ed.* **2018**, *57*, 10123–10126; b) K. Xiao, P. Giusto, L. P. Wen, L. Jiang, M. Antonietti, *Angew. Chem. Int. Ed.* **2018**, *57*, 10123–10126.

[9] a) S. Hong, J. K. El-Demellawi, Y. Lei, Z. Liu, F. A. Marzooqi, H. A. Arafat, H. N. Alshareef, *ACS Nano* **2022**, *16*, 792–800; b) L. Ding, D. Xiao, Z. Lu, J. Deng, Y. Wei, J. Caro, H. Wang, *Angew. Chem. Int. Ed.* **2020**, *59*, 8720–8726; c) Z. Zhang, S. Yang, P. Zhang, J. Zhang, G. Chen, X. Feng, *Nat. Commun.* **2019**, *10*, 2920; d) R. Qu, X. Zeng, L. Lin, G. Zhang, F. Liu, C. Wang, S. Ma, C. Liu, H. Miao, L. Cao, *ACS Nano* **2020**, *14*, 16654–16662.

[10] H. Qian, D. Wei, Z. L. Wang, *Nano Res.* **2023**, *16*, 11718–11730.

[11] a) H. Zhan, Z. Xiong, C. Cheng, Q. Liang, J. Z. Liu, D. Li, *Adv. Mater.* **2020**, *32*, 1904562; b) X. Liang, J. Tang, Y. Zhong, B. Gao, H. Qian, H. Wu, *Nat. Electron.* **2024**, *7*, 193–206; c) P. Peng, H. Qian, J. Liu, Z. Wang, D. Wei, *Int. J. Smart Nano Mater.* **2024**, *15*, 198–221; d) L. Cao, F. Xiao, Y. Feng, W. Zhu, W. Geng, J. Yang, X. Zhang, N. Li, W. Guo, L. Jiang, *Adv. Funct. Mater.* **2017**, *27*, 1604302.

[12] a) H. B. Park, J. Kamcev, L. M. Robeson, M. Elimelech, B. D. Freeman, *Science* **2017**, *356*, eaab0530; b) F. Xiao, D. Ji, H. Li, J. Tang, Y. Feng, L. Ding, L. Cao, N. Li, L. Jiang, W. Guo, *Mater. Chem. Front.* **2018**, *2*, 935–941.

[13] L. Bocquet, *Nat. Mater.* **2020**, *19*, 254–256.

[14] A. Butturini, P. Herzsprung, O. J. Lechtenfeld, S. Venturi, S. Amalfitano, E. Vazquez, N. Pacini, D. M. Harper, F. Tassi, S. Fazi, *Water Res.* **2020**, *173*, 115532.

[15] a) Z. Zhou, J. Yang, H. Lv, T. Zhou, J. Zhao, H. Bai, F. Pu, P. Xu, *Genome Biol. Evol.* **2023**, *15*; b) F. Sui, S. Zang, Y. Fan, H. Ye, *PLoS One* **2016**, *11*, e0164734.

[16] Y. Zhou, L. Jiang, *Joule* **2020**, *4*, 2244–2248.

[17] a) W. H. Schlesinger, S. Jasechko, *Agric. For. Meteorol.* **2014**, *189–190*, 115–117; b) A. J. McElrone, B. Choat, G. A. Gambetta, C. R. Brodersen, *Nature Education Knowledge* **2013**, *4*, 6; c) T. Xu, Z. Li, S. Bao, Y. Su, Z. Su, S. Zhi, E. Zheng, *PLoS One* **2023**, *18*, e0281080.

[18] a) A. A. Myburg, R. R. Sederoff, *Encyclopedia of Life Sciences.* **2013**, DOI: 10.1038/npg.els.0001302; b) F. Wang, Z. Wang, X. Meng, X. Wang, Y. Fan, Y. Jin, W. Zhang, N. Yang, *J. Membr. Sci.* **2023**, *686*, 121975.

[19] A. R. Koltonow, J. Huang, *Science* **2016**, *351*, 1395–1396.

[20] Z. Zhang, W. Shen, L. Lin, M. Wang, N. Li, Z. Zheng, F. Liu, L. Cao, *Adv. Sci.* **2020**, *7*, 2000286.

[21] a) S. Hong, F. Ming, Y. Shi, R. Li, I. S. Kim, C. Y. Tang, H. N. Alshareef, P. Wang, *ACS Nano* **2019**, *13*, 8917–8925; b) G. Song, Y. Zhan, Y. Hu, J. Rao, N. Li, Z. Wu, Z. Su, B. Lü, R. Liu, B. Jiang, G. Chen, F. Peng, *Adv. Funct. Mater.* **2023**, *33*, 2214044.

[22] a) J. Shen, G. Liu, Y. Ji, Q. Liu, L. Cheng, K. Guan, M. Zhang, G. Liu, J. Xiong, J. Yang, W. Jin, *Adv. Funct. Mater.* **2018**, *28*, 1801511; b) L. Ding, Y. Wei, L. Li, T. Zhang, H. Wang, J. Xue, L.-X. Ding, S. Wang, J. Caro, Y. Gogotsi, *Nat. Commun.* **2018**, *9*, 155.

[23] a) J. Yan, C. E. Ren, K. Maleski, C. B. Hatter, B. Anasori, P. Urbankowski, A. Sarycheva, Y. Gogotsi, *Adv. Funct. Mater.* **2017**, *27*, 1701264; b) G. R. Berdiyorov, *AIP Adv.* **2016**, *6*; c) X. Xie, K. Kretschmer, B. Anasori, B. Sun, G. Wang, Y. Gogotsi, *ACS Appl. Nano Mater.* **2018**, *1*, 505–511.

[24] S. Kim, S. Choi, H. G. Lee, D. Jin, G. Kim, T. Kim, J. S. Lee, W. Shim, *Nat. Commun.* **2021**, *12*, 47.

[25] W. Guo, L. Cao, J. Xia, F.-Q. Nie, W. Ma, J. Xue, Y. Song, D. Zhu, Y. Wang, L. Jiang, *Adv. Funct. Mater.* **2010**, *20*, 1339–1344.

[26] D.-K. Kim, C. Duan, Y.-F. Chen, A. Majumdar, *Microfluid. Nanofluid.* **2010**, *9*, 1215–1224.

[27] a) W. Guo, C. Cheng, Y. Wu, Y. Jiang, J. Gao, D. Li, L. Jiang, *Adv. Mater.* **2013**, *25*, 6064–6068; b) J. Ji, Q. Kang, Y. Zhou, Y. Feng, X. Chen, J. Yuan, W. Guo, Y. Wei, L. Jiang, *Adv. Funct. Mater.* **2017**, *27*, 1603623.

[28] L. Chang, T. Zhang, F. Wang, H. Ma, W. Xie, T. Ding, X. Xiao, *2D Mater.* **2023**, *10*, 014009.

[29] V. Natu, M. Sokol, L. Verger, M. W. Barsoum, *J. Phys. Chem. C* **2018**, *122*, 27745–27753.
[30] S. Wang, Z. Wang, Y. Fan, X. Meng, F. Wang, N. Yang, *J. Membr. Sci.* **2023**, *668*, 121203.
[31] a) E. R. Nightingale Jr., *J. Phys. Chem.* **1959**, *63*, 1381–1387; b) Q. Wen, D. Yan, F. Liu, M. Wang, Y. Ling, P. Wang, P. Kluth, D. Schauries, C. Trautmann, P. Apel, W. Guo, G. Xiao, J. Liu, J. Xue, Y. Wang, *Adv. Funct. Mater.* **2016**, *26*, 5796–5803.
[32] Z. Lu, Y. Wei, J. Deng, L. Ding, Z.-K. Li, H. Wang, *ACS Nano* **2019**, *13*, 10535–10544.
[33] R. B. Schoch, J. Han, P. Renaud, *Rev. Mod. Phys.* **2008**, *80*, 839–883.

Manuscript received: August 7, 2024
Accepted manuscript online: August 15, 2024
Version of record online: October 16, 2024